Alma Mater Studiorum · Università di Bologna

Dipartimento di Fisica e Astronomia "Augusto Righi"
Corso di Laurea in Fisica

Long-range effects on dark matter self interactions in clusters and dwarf galaxies

Relatore:
Prof. Filippo Sala

Presentata da:
Francesco Rastelli

Anno Accademico 2025/2026

Abstract

Il modello cosmologico standard descrive con successo l'evoluzione dell'Universo su scale cosmologiche, ma presenta persistenti discrepanze su scale galattiche (i cosiddetti "small scale puzzles"). Una possibile soluzione consiste nel superare l'assunzione di materia oscura (MO) priva di collisioni, introducendo l'ipotesi della MO Auto-Interagente (SIDM).

L'obiettivo di questa tesi è l'analisi di modelli SIDM con sezioni d'urto dipendenti dalla velocità. Il calcolo di tali sezioni d'urto richiede dispendiose integrazioni numeriche, dovute alla risoluzione dello scattering quantistico nel potenziale di Yukawa non-relativistico, indotto dall'interazione ipotizzata fra le particelle di MO. La tesi si concentra quindi sullo sviluppo di approssimazioni analitiche, trattando l'effetto quantistico non-relativistico del Sommerfeld enhancement. Dal limite di Coulomb, si esamina successivamente il potenziale di Hulthén, che approssima quello di Yukawa ammettendo una soluzione analitica esatta in onda-s.

Le sezioni d'urto calcolate vengono confrontate con i vincoli osservativi provenienti dalle galassie nane (velocità relativa delle particelle di MO $\sim$ 30 km/s) e dagli ammassi di galassie ($\sim$ 1000 km/s). Evidenziando i limiti cinematici dell'approssimazione in onda-s ad alte velocità, si costruisce un modello fenomenologico che raccorda il regime di bassa velocità col limite perturbativo di Born. Quantitativamente, assumendo una massa di MO $m_\chi = 15$ GeV, si dimostra che un mediatore leggero con $m_\phi \approx 50$ MeV predice i dati su scale multiple: esso genera l'ampia sezione d'urto, richiesta dalla risoluzione dei "small scale puzzles", nelle galassie nane ($\sigma/m_\chi \sim 1.5$ cm^2/g) grazie all'effetto Sommerfeld, garantendo la forte soppressione Rutherford ($\lesssim 0.1$ cm^2/g) negli ammassi galattici. Infine, si discutono i limiti dell'approccio e le estensioni per una descrizione rigorosa della dinamica degli aloni oscuri.

Contents

Chapter 1

Basic concepts of Dark Matter

1.1 Evidence for Dark Matter

1.1.1 Historical Introduction

The hypothesis of unobservable mass has deep historical roots. Initially, scientists like Lord Kelvin proposed the existence of "dark bodies", while early 20th-century astronomers like Jacobus Kapteyn and Jan Oort modeled the Galaxy's mass distribution. Oort concluded that the inferred total density in the local galactic disk (on scales of hundreds of parsecs around the Sun) exceeded the contribution of visible stars, attributing this missing matter to faint stars and nebulous material [1]. However, the modern concept of Dark Matter (DM) particles developed only when clear observational evidence emerged across several astronomical scales [2].

1.1.2 Modern Observational Evidence: Galactic Rotation Curves

A definitive breakthrough came from the kinematic study of spiral galaxies using 21-cm radio emission from neutral hydrogen. According to Newtonian dynamics, the circular velocity $v_{\rm circ}$ of tracers outside the luminous disk should exhibit a Keplerian decline:

$$v_{\rm circ} = \sqrt{\frac{GM(r)}{r}} \tag{1.1}$$

Instead, observations showed rotation curves remaining constant at large radii [3]. One historically significant example can be seen in Fig. 1.1. To maintain this flat velocity profile, the enclosed mass must increase linearly with the radius, implying a density profile $\rho(r) \propto r^{-2}$. As astronomer Ken Freeman noted in 1970, this discrepancy definitively proved the existence of an extended, non-luminous DM halo influencing star motion in galaxies [4, 1].

1.1.3 Modern Observational Evidence: Galaxy Clusters

On larger scales, galaxy clusters serve as excellent probes for dark matter. In 1933, Fritz Zwicky provided early evidence for DM by applying the virial theorem to the Coma cluster, revealing that the mass required to keep the high-velocity galaxies gravitationally bound substantially exceeded the visible mass [7, 8].

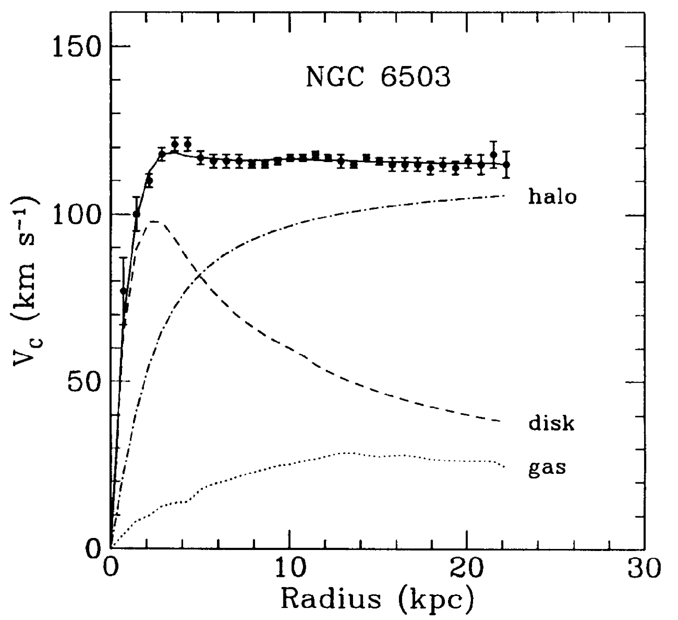

Figure 1.1: *Rotation curve of the spiral galaxy NGC 6503. The measured circular velocities (data points with error bars) remain flat at large radii, in contrast with the expected Keplerian decline. The dashed lines represent the Newtonian contributions computed from the visible gas and the stellar disk. The solid line shows the total rotation curve obtained by including a Dark Matter halo, which effectively fits the observational data. Figure adapted from [5], based on original data by Begeman et al. [6].*

To understand Zwicky's approach, consider the Virial Theorem for a stable, self-gravitating system:

$$2\langle T\rangle = -\langle V\rangle \tag{1.2}$$

which for a Newtonian potential ($V \propto -1/r$) gives:

$$\langle T\rangle = \frac{1}{2}|\langle V\rangle| \tag{1.3}$$

The radius of the Coma cluster can be estimated from its angular size $\theta \sim 1^\circ \simeq \frac{\pi}{180}$ rad and its distance $d \sim 100$ Mpc:

$$R = \theta \cdot d \sim 1.75 \text{ Mpc} \sim 5.4 \times 10^{19} \text{ km} \tag{1.4}$$

The mean kinetic and potential energies of the cluster are:

$$\langle T\rangle = \frac{1}{2}Mv^2, \quad |\langle V\rangle| \sim \frac{GM^2}{R} \tag{1.5}$$

Assuming spherical symmetry, the 3D velocity squared is $v^2 = 3v_{\text{disp}}^2$, where $v_{\text{disp}} \sim$ 1000 km/s is the observed velocity dispersion of the galaxies along the line of sight. Applying the Virial Theorem yields:

$$\frac{1}{2}M(\sqrt{3}v_{\text{disp}})^2 = \frac{1}{2}\frac{GM^2}{R} \implies \boxed{M = \frac{3v_{\text{disp}}^2 R}{G} \sim 24 \times 10^{44} \text{ kg} \sim 12 \times 10^{14} M_\odot} \tag{1.6}$$

This inferred mass is one order of magnitude larger than the mass of the observable matter ($M_{\text{obs}} \sim 10^{14} M_\odot$ [1]), providing clear evidence for an unseen mass component.

This conclusion remains true despite the approximations employed, such as neglecting the discrete nature of the galaxy distribution [2].

Today, precision measurements of cluster masses no longer rely solely on galaxy kinematics, but rather on X-ray emissions from hot intergalactic gas ($T \sim 10^8$ K). By analyzing the thermal *bremsstrahlung* spectrum and assuming hydrostatic equilibrium, the total gravitating mass can be accurately reconstructed, confirming Zwicky's early DM predictions [2].

1.1.4 Modern Observational Evidence: The Bullet Cluster

A striking empirical proof for the existence of collisionless DM comes from merging galaxy systems, most notably the Bullet Cluster (1E0657-558). In 2006, Clowe et al. mapped the system's mass distribution using weak gravitational lensing [9].

As shown in Fig. 1.2, the observations revealed an evident physical offset: the bulk of the baryonic matter (the hot, X-ray emitting gas that collided and slowed down) is spatially separated from the total mass distribution reconstructed via lensing. This offset proves that an unseen, collisionless component must dominate the gravitational potential, passing through the collision without experiencing drag [9].

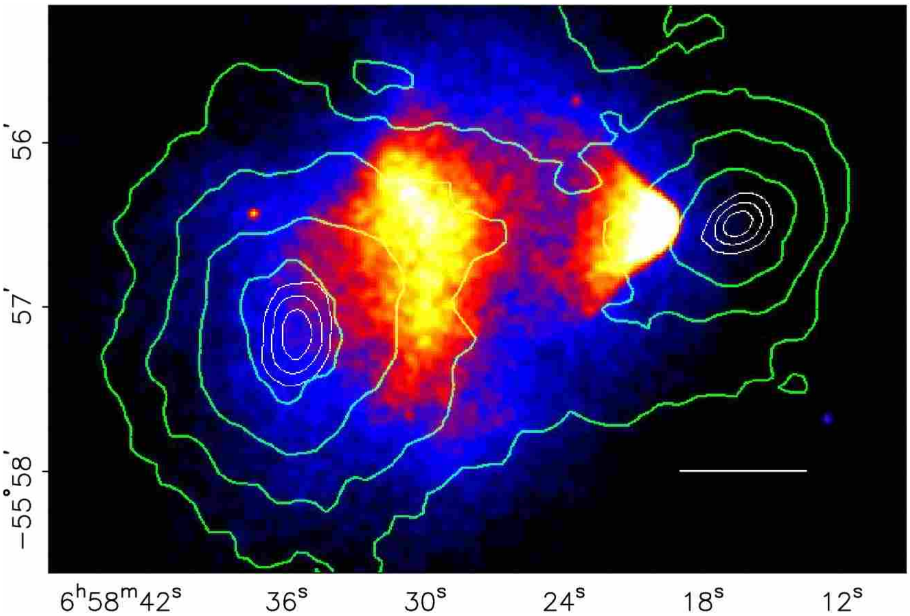

Figure 1.2: *Composite view of the merging cluster system known as the Bullet Cluster. The underlying color map displays X-ray data from a 500 ks Chandra exposure, while the green contours represent the mass distribution as reconstructed through (weak) gravitational lensing. The white horizontal bar indicates a scale of 200 kpc. Adapted from Ref. [9].*

1.1.5 Modern Observational Evidence: Cosmic Microwave Background

At the cosmological scale, the most compelling evidence for Dark Matter comes from the Cosmic Microwave Background (CMB). The CMB is the relic radiation from the epoch of recombination[1]. In the primordial plasma, there were tiny 3D density fluctuations, known

[1] Recombination is the epoch, approximately 380,000 years after the Big Bang, when the Universe cooled enough for protons and electrons to combine into neutral hydrogen atoms. This decoupled matter from radiation, allowing photons to travel freely and forming the CMB [2].

as inhomogeneities. Today, we observe the projection of these physical fluctuations on the sky as minuscule 2D temperature variations ($\delta T/T \sim 10^{-5}$), which are called CMB anisotropies.

These anisotropies, and the subsequent formation of cosmic structures, can only be explained by incorporating Dark Matter [2]. Before recombination, baryons and photons formed a tightly coupled fluid. Gravity pulled matter inward, while radiation pressure pushed it outward, creating pressure waves known as "acoustic oscillations"[2]. Dark Matter, however, does not interact with photons. Unaffected by radiation pressure, it collapsed much earlier, forming dense initial clumps. After recombination, baryons decoupled from photons and fell into these pre-existing DM overdensities, which acted as gravitational wells for future galaxies. Without Dark Matter, structures would not have formed in time [2].

Ultimately, these cosmological observations, along with several others discussed in detail in Ref. [2],confirm the necessity of non-interacting Dark Matter and provide the most precise measurement of its density today.

1.2 Alternative to Dark Matter: Modified Gravity

As an alternative to DM, Mordehai Milgrom proposed Modified Newtonian Dynamics (MOND) in 1982 [10]. MOND attempts to explain astrophysical anomalies by modifying Newton's laws at very low accelerations (quantitatively, for $a \ll a_0 \sim 10^{-12}$ m/s^2).

Initially, this theory had one major problem: it failed to conserve basic physical quantities such as energy, momentum, or angular momentum. To resolve these inconsistencies, the framework evolved into AQUAL (AQUAdratic Lagrangian theory). By modifying the Newtonian Lagrangian rather than the force law directly, AQUAL successfully restored these conservation laws [1].

While these early MOND formulations successfully reproduce galactic-scale observables, such as rotation curves and the Tully-Fisher relation[3], they remained fundamentally non-relativistic [1]. In order to explain relativistic phenomena like cosmological expansion and gravitational lensing, MOND had to be further embedded into relativistic scalar-tensor frameworks, culminating in theories like RAQUAL and Bekenstein's TeVeS (Tensor-Vector-Scalar) theory [1].

Despite these advancements, embedding MOND into a relativistic framework introduced a new set of theoretical and observational contradictions. To prevent violations of causality (such as superluminal motion of the scalar field), these theories required modifications that directly compromised their consistency with high-precision solar system tests. Furthermore, relativistic MOND fails on the scale of galaxy clusters. In General Relativity, gravitational lensing depends on the total mass-energy tensor, whereas in relativistic MOND formulations, the magnitude of lensing is strictly proportional to the visible baryonic mass. Since the observed deflection of light around galaxy clusters is vastly greater than what baryonic mass alone can produce, significant unseen mass is still mathematically required

[2] The "acoustic peaks" in the CMB power spectrum are essentially a frozen record of these pressure waves at the exact moment of recombination. By analyzing their relative heights, cosmologists can isolate the purely gravitational pull of total matter from the scattering effects of baryons [2].

[3] The Tully-Fisher relation is an empirical relationship between the intrinsic luminosity (L) of a spiral galaxy and its rotation velocity ($V_{\rm rot}$), typically expressed as $L \propto V_{\rm rot}^{\alpha}$ where $\alpha \approx 4$. In astronomy, it is used mainly as a tool to estimate the distance of galaxies [1].

for a correct description of the phenomenon, resulting in MOND being incomplete at these scales [1].

Moreover, a definitive challenge to MOND and purely modified gravity theories comes from the Bullet Cluster (discussed in Sec. 1.1.4): the spatial separation between baryonic gas and the gravitational potential rules out theories that attempt to trace gravity solely back to visible matter.

Ultimately, the most precise and compelling evidence for Dark Matter does not come from galactic observables but from cosmological observations of the CMB and structure formation. On cosmological scales, MOND cannot make reliable predictions. As discussed in Sec. 1.1.5, DM instead acts as a gravitational catalyst for cosmic evolution: without it, primordial density fluctuations could not have collapsed to form the galaxies we observe today. Ordinary baryonic matter alone could not have driven this process due to its early coupling with radiation, which completely suppressed its initial clustering [2, Chaps 1, 11].

1.3 What is Dark Matter?

In the standard ΛCDM cosmological framework, Dark Matter (DM) is operationally defined as a pressureless fluid characterized by the following properties [2]:

- **Matter:** It behaves macroscopically as a pressureless fluid (equation of state $w = 0$)[4], with its density scaling inversely with the expanding volume.
- **Cold:** It was non-relativistic at the epoch of matter-radiation equality, a condition that allowed the particles to cluster and seed structure formation.
- **Stable:** Its lifetime vastly exceeds the current age of the Universe (~ 13.8 Gyr).
- **Adiabatic:** It shares the same primordial density inhomogeneities as ordinary matter and photons.
- **Collision-less and Dissipation-less:** Its interactions with ordinary matter, light, and itself are phenomenologically negligible. Lacking electromagnetic interactions, it cannot dissipate energy via radiation.

While weak-scale interactions may be theoretically required for the early-universe production of DM, they remain irrelevant on macroscopic astrophysical scales [2].

However, relying exclusively on this collision-less ΛCDM leads to various problems regarding the internal dynamics of dwarf galaxies and satellites. The next chapter will address these so-called "small-scale puzzles", motivating the need to move beyond purely non-interacting assumptions and setting the stage for phenomena such as the Sommerfeld enhancement.

[4]The parameter w relates the pressure p and the energy density ρ through the equation of state $p = w\rho c^2$. For non-relativistic matter, the pressure is negligible ($w \approx 0$). Consequently, according to the FLRW metric, the density scales as $\rho \propto a^{-3(1+w)}$; for $w = 0$ we recover the standard dilution $\rho \propto a^{-3}$, where a is the cosmological scale factor [2, Appendix C.2].

Chapter 2

Dark Matter self-interactions

2.1 Open issues in small-scale structure formation

While the collisionless ΛCDM paradigm is successful on large scales ($\gtrsim \mathcal{O}(\mathrm{Mpc})$), high-resolution N-body simulations containing only DM highlight open questions when compared with observations on galactic and sub-galactic scales. Notable discrepancies include [11]:

- **Core-cusp problem:** DM-only simulations predict a steeply peaked Navarro-Frenk-White (NFW) density profile,

$$\rho_{\mathrm{NFW}}(r) = \frac{\rho_s}{(r/r_s)(1 + r/r_s)^2} \implies \rho \propto r^{-1} \text{ for } r \to 0 \tag{2.1}$$

  where r_s is the scale radius and ρ_s is the characteristic density. However, kinematic observations of dwarf galaxies strongly favor a flat, “cored” inner profile ($\rho \propto r^0$).

- **Diversity problem:** Galaxies with identical maximal circular velocities exhibit a wide scatter in their inner rotation curves, contradicting the uniform, self-similar halos predicted by simulations.

- **Missing satellites problem:** The Local Group contains orders of magnitude fewer observed satellite galaxies than the massive subhalo abundance predicted by hierarchical clustering.

- **Too-big-to-fail (TBTF) problem:** The most massive predicted subhalos are theoretically dense enough to trigger star formation, yet their central densities exceed those inferred from the observed brightest Milky Way satellites.

One possible way to solve these problems is to consider baryonic matter in the simulations. Historically, due to computational limits, N-body simulations were “DM-only”. However, recent high-precision simulations (called baryonic or hydrodynamical simulations) have begun to implement ordinary matter, recognizing its significant role in galaxy formation. These simulations must account for a large number of multi-scale physical processes, including gas cooling, radiation, magnetic fields, and star formation. Furthermore, they introduce the dynamics of stellar feedback, such as supernovae or supermassive black holes. These highly energetic events can drive massive gas outflows, causing rapid fluctuations in the local gravitational potential. This process transfers energy to the dark matter particles, potentially moving matter away from the galactic center and transforming a dense NFW cusp into the flat core favored by observations [2].

Despite these successes, hydrodynamical simulations present significant challenges. The physical processes determining the behavior of the baryons often occur on scales much smaller than the spatial resolution of the computer codes. Therefore, they rely heavily on phenomenological models with freely adjustable parameters. This introduces the risk of over-fitting: it can be difficult to understand whether the successful reproduction of a galaxy is a consequence of the underlying physics or only a consequence of adjusted numerical parameters compensating for other effects [2].

Given the theoretical uncertainties associated with baryonic feedback, it remains unclear whether ordinary matter alone can fully resolve these small-scale puzzles. Rather than relying entirely on complex baryonic astrophysics, this chapter explores a significant modification to a fundamental DM property: abandoning the collisionless hypothesis. By introducing Self-Interacting Dark Matter (SIDM), we investigate a solely dark mechanism to address these galactic anomalies [2].

2.2 Self-Interacting DM as a possible solution

Self-Interacting Dark Matter (SIDM) introduces non-gravitational elastic $\chi\chi \to \chi\chi$ collisions, where χ is the DM particle [12]. Unlike collisionless CDM, these interactions transport heat inward, thermalizing the dense inner halo. This thermalization occurs where the scattering rate $\Gamma = \rho(\sigma/m)v_{\rm rel}$ times the halo age $t_{\rm age}$ exceeds unity:

$$\Gamma t_{\rm age} \approx \left(\frac{\rho}{0.1\ M_\odot/{\rm pc}^3}\right)\left(\frac{\sigma/m}{1\ {\rm cm}^2/{\rm g}}\right)\left(\frac{v_{\rm rel}}{50\ {\rm km/s}}\right)\left(\frac{t_{\rm age}}{10\ {\rm Gyr}}\right) \gtrsim 1 \tag{2.2}$$

This process creates an isothermal core with a Maxwell-Boltzmann velocity distribution, lowers the central density, and isotropizes the halo shape (see Fig. 2.1).

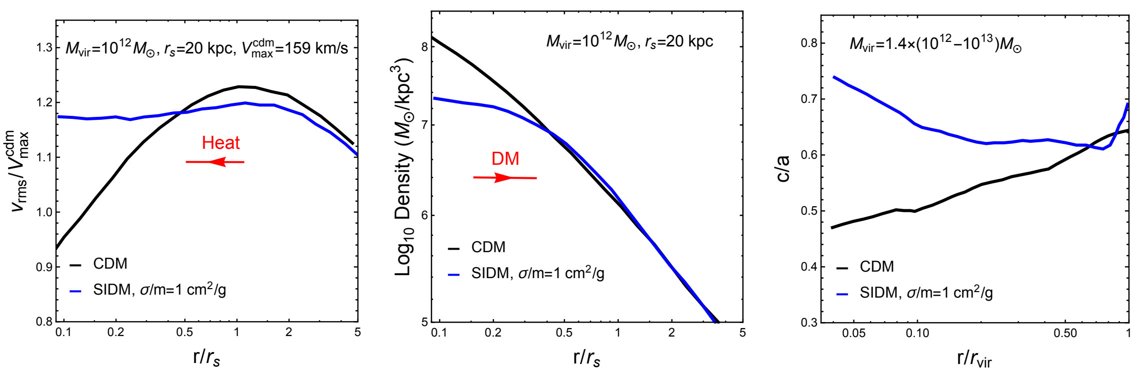

(a) *Velocity dispersion* **(b)** *Density profile* **(c)** *Halo shape (c/a)*

Figure 2.1: *Comparison between CDM (black) and SIDM (blue) halo properties. (a) Isothermalization of the inner halo; (b) formation of a central core; (c) isotropization of the halo shape toward the center. Adapted from [11], based on original simulation data by Rocha et al. [13] and Peter et al. [14].*

To quantitatively address the small-scale puzzles, N-body simulations indicate that cross-sections in the broad range of $\sigma/m \approx 0.5 - 50\ \ {\rm cm}^2/{\rm g}$ are successful on galactic scales. Specifically, these values produce $\mathcal{O}(1\ {\rm kpc})$ cores in dwarf galaxies (where typical relative velocities are $v_{\rm rel} \sim 30 - 50$ km/s [1]), addressing both the core-cusp and the too-big-to-fail (TBTF) problems [11, Sec. 3.B].

[1] Literature often parameterizes halo kinematics via the 1D velocity dispersion σ_v (frequently denoted

However, this requirement must be compared with constraints deriving from larger scales. In massive systems like galaxy clusters, relative velocities are much higher, and the cross-section is strictly bounded by observations of cluster mergers. Let us consider the probability P that a DM particle from the main cluster scatters while crossing the target sub-cluster:

$$P = \int \frac{\sigma_{\rm self}}{m_\chi} \rho_2 \, dx = \frac{\sigma_{\rm self}}{m_\chi} \Sigma_2 \tag{2.3}$$

where Σ_2 is the target's surface mass density. In the case of the Bullet Cluster ($v_{\rm rel} \sim 3000$ km/s), the dark matter halos passed through each other without significant deceleration. Requiring a low scattering probability ($P \lesssim 0.3$) and using the observed central surface mass density $\Sigma_2 \approx 0.3$ g/cm^2 [15, Secs. 2.2 and 2.3], we obtain an indicative upper limit:

$$\frac{\sigma_{\rm self}}{m_\chi} \lesssim \frac{P}{\Sigma_2} \implies \boxed{\frac{\sigma_{\rm self}}{m_\chi} \lesssim 1 \ {\rm cm}^2/{\rm g}} \tag{2.4}$$

While the Bullet Cluster limit might allow a valid value for a constant cross-section, the assumption fails when considering galaxy clusters in equilibrium. Observations of cluster ellipticity and strong lensing in these systems ($v_{\rm rel} \sim 1000$ km/s) impose a much stricter limit of $\sigma/m \lesssim 0.1$ cm^2/g to avoid the isotropization[2] of the inner halo [11, Sec. 3.C]. Therefore, a single constant cross-section cannot simultaneously satisfy the high values required by dwarfs ($0.5 - 50$ cm^2/g) and the upper bounds of relaxed clusters (< 0.1 cm^2/g). A possible solution to this contrast is provided by velocity-dependent SIDM models, where the interaction rate is large at low velocities to resolve small-scale puzzles, but suppressed at high velocities to satisfy all cluster constraints.

Moreover, while self-interactions relieve the core-cusp and TBTF issues, they do not resolve all discrepancies mentioned in Sec. 2.1. Most notably, allowed SIDM cross-sections leave the subhalo mass function largely unchanged, meaning SIDM alone cannot solve the missing satellites problem [11, Sec. 3.D].

Finally, similarly to Sec. 2.1, baryons can be implemented in SIDM simulations, although they introduce significant uncertainties [11]. Baryonic feedback can simulate SIDM effects, producing similar observational outcomes, making it difficult to distinguish which mechanism is truly responsible. Until these baryonic processes are better understood, it remains difficult to make definitive claims about SIDM on small scales [11, Sec. 3.E].

2.3 Particle Physics Models

In Dark Matter (DM) models featuring long-range forces, forward-scattering divergences make numerical simulations computationally expensive for halo core formation. To find particle parameters in macroscopic halo dynamics, simulations rely on effective proxy cross-sections (such as the transfer or viscosity cross-sections)[3] that isolate the relevant momentum exchange [11].

simply as v). Assuming a Maxwell-Boltzmann velocity distribution [11, Sec. 7.B], the mean relative velocity is $\langle v_{\rm rel} \rangle = \frac{4}{\sqrt{\pi}} \sigma_v \approx 2.26 \sigma_v$ (as explicitly derived in Appendix A). Since they differ only by an $\mathcal{O}(1)$ factor, we safely use $v_{\rm rel}$ directly for our order-of-magnitude estimates.

[2] Standard collisionless dark matter forms triaxial (ellipsoidal) halos. Self-interactions scatter particles, equalizing the velocity dispersion in all directions and forcing the inner mass distribution into a spherical shape.

[3] The momentum transfer cross-section is defined as $\sigma_T = \int (1 - \cos\theta) \frac{d\sigma}{d\Omega} d\Omega$, which suppresses forward scattering ($\theta \sim 0$). The viscosity (or conduction) cross-section is defined as $\sigma_V = \int \sin^2\theta \frac{d\sigma}{d\Omega} d\Omega$, which suppresses both forward and backward scattering, isolating perpendicular momentum transfer.

Furthermore, these studies reveal that a constant cross-section cannot simultaneously explain core formation in dwarf galaxies and satisfy the bounds of massive galaxy clusters. The effective self-interaction cross-section must therefore be velocity-dependent, a feature that naturally arises in light mediator models [11].

2.3.1 Light mediator models

Assuming DM is charged under a broken $U(1)$ gauge symmetry, self-interactions can be mediated by a light vector or scalar boson of mass m_ϕ, yielding a Yukawa potential:

$$V(r) = \pm \frac{\alpha_\chi}{r} e^{-m_\phi r} \tag{2.5}$$

where α_χ is the dark fine structure constant.

To understand how a velocity-dependent cross-section naturally emerges in this framework, it is instructive to look at the perturbative Born limit ($\alpha_\chi m_\chi / m_\phi \ll 1$), where the differential cross-section is explicitly given by [11]:

$$\frac{d\sigma}{d\Omega} = \frac{\alpha_\chi^2 m_\chi^2}{[m_\chi^2 v_{\rm rel}^2 (1 - \cos\theta)/2 + m_\phi^2]^2} \tag{2.6}$$

This analytical expression demonstrates directly how the scattering scales depending on the relative velocity $v_{\rm rel}$ compared to the mediator mass scale m_ϕ. Specifically:

- **Low-velocity limit** ($m_\chi v_{\rm rel} \ll m_\phi$)**:** The m_ϕ^2 term dominates the denominator. The interaction behaves as a contact interaction, and the cross-section is velocity-independent (constant).
- **High-velocity limit** ($m_\chi v_{\rm rel} \gg m_\phi$)**:** The $v_{\rm rel}^2$ term dominates the denominator. The interaction is long-range, and the cross-section scales as $\propto 1/v_{\rm rel}^4$ (Rutherford regime).

By introducing a small but finite mediator mass, the transition between these two limits can be set to occur at intermediate velocities ($v_{\rm rel} \sim 300$ km/s). This implies a mass ratio $m_\phi/m_\chi \sim v_{\rm rel}/c \sim 10^{-3}$, which keeps the scattering rate high at the low velocities of dwarf galaxies (contact regime) while heavily suppressing it at the high velocities of galaxy clusters (Rutherford regime), simultaneously resolving multi-scale observations [11].

However, while the Born approximation illustrates the fundamental mechanism, exploring the parameter space favored by observations (Fig. 2.2) typically requires stronger couplings. In such cases, the perturbative limit is no longer sufficient, and a complete description must incorporate non-perturbative phenomena, where multiple scatterings become important [11].

2.4 Phenomenological Setup for Dark Matter Self-Interactions

In this work, we consider a model in which Dark Matter (DM) is composed of particles χ with mass m_χ. These particles self-interact through the exchange of a dark mediator ϕ, belonging to a Beyond Standard Model (BSM) sector, with mass m_ϕ.

The strength of this interaction is determined by a dark coupling constant $\alpha_\chi \equiv g_\chi^2/(4\pi)$, where g_χ represents the coupling between the DM particle and the mediator. Since the exact computation of the $\chi\bar{\chi} \to \chi\bar{\chi}$ scattering process requires the formalism of Quantum

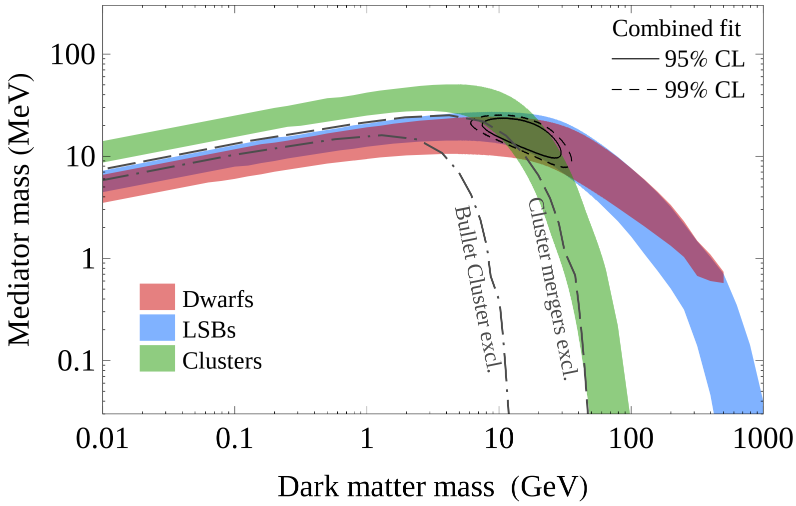

Figure 2.2: *Preferred parameter space* (m_χ, m_ϕ) *for a repulsive Yukawa SIDM model with* $\alpha_\chi \approx 1/137$. *The colored bands indicate the regions favored by dwarf galaxies (red), LSB (Low Surface Brightness) galaxies (blue), and galaxy clusters (green) at* 95% *CL. The black solid contour reveals a closed common region that satisfies all constraints simultaneously. Reprinted from [16].*

Field Theory (QFT), we take the analytical cross-section derived in the literature for this model as our starting point [17][4].

The self-interacting cross-section is simply given by:

$$\sigma_{\chi\bar{\chi}\to\chi\bar{\chi}} = 8\pi\alpha_\chi^2 \frac{m_\chi^2}{m_\phi^4}\left[\frac{1}{1+r} - \frac{\ln(1+r)}{r(r+2)}\right] \tag{2.7}$$

where r is a dimensionless kinematic parameter defined as:

$$r = \left(\frac{v_{\rm rel} m_\chi}{m_\phi}\right)^2 \tag{2.8}$$

with $v_{\rm rel}$ being the relative velocity between the interacting DM particles [17].

Before proceeding with the numerical evaluation, we briefly introduce the choice of benchmark parameters. We adopt a Dark Matter mass of $m_\chi = 1$ GeV as a benchmark to investigate the Light Dark Matter (LDM) scenario. It must be recalled that small-scale anomalies can be resolved by a wide range of DM masses, since the cross-section depends simultaneously on multiple parameters such as m_χ, m_ϕ, and α_χ. For this specific exercise, the target is to find the mediator mass in order to achieve a cross-section of $\sigma/m_\chi \sim 1$ cm^2/g, which acts as a typical reference value capable of forming density cores in dwarf galaxies [11].

The dark coupling is set to $\alpha_\chi = 0.1$ to ensure a perturbative regime. Finally, we consider the non-relativistic approximation ($v_{\rm rel} \ll c$): DM relative velocity dispersions range from ~ 10 km/s in dwarf galaxies to ~ 1500 km/s in clusters ($v_{\rm rel}/c \sim 10^{-5} - 10^{-3}$), making relativistic effects negligible.

[4]Notice that Eq. (2.7) differs by an overall factor of 2 compared to the result in Ref. [17]. This is due to the fact that they assume the Dark Matter particle to be its own antiparticle, while in our scenario χ and $\bar{\chi}$ are distinct particles.

Thanks to these assumptions, we can estimate the mediator mass m_ϕ that satisfies the cross-section constraint. Taking advantage of the non-relativistic limit $v_{\rm rel} \ll c$, the dimensionless parameter $r = (v_{\rm rel} m_\chi / m_\phi)^2$ becomes vanishingly small ($r \ll 1$).

Taking the leading-order Taylor expansion of Eq. (2.7) for $r \to 0$, the term in brackets simplifies to 1/2. In this regime, the cross-section becomes independent of the relative velocity (Born limit):

$$\sigma_{\chi\bar{\chi}\to\chi\bar{\chi}} \approx 8\pi\alpha_\chi^2 \frac{m_\chi^2}{m_\phi^4}\left(\frac{1}{2}\right) = 4\pi\alpha_\chi^2 \frac{m_\chi^2}{m_\phi^4} \tag{2.9}$$

By inverting this relation, we can explicitly solve for the required mediator mass:

$$m_\phi = \left(4\pi\alpha_\chi^2 \frac{m_\chi^2}{\sigma_{\chi\bar{\chi}\to\chi\bar{\chi}}}\right)^{1/4} \tag{2.10}$$

Substituting the benchmark values $\alpha_\chi = 0.1$, $m_\chi = 1$ GeV, and the target cross-section $\sigma/m_\chi = 1\ \text{cm}^2/\text{g}$ (converted into natural units GeV^{-3}), we obtain a mediator mass of $m_\phi \approx 72.4$ MeV.

To verify the validity of this benchmark across all astronomical scales, we evaluate the full theoretical cross-section (Eq. (2.7), keeping the exact dependence on r) as a function of the relative velocity and compare it with the observational data.

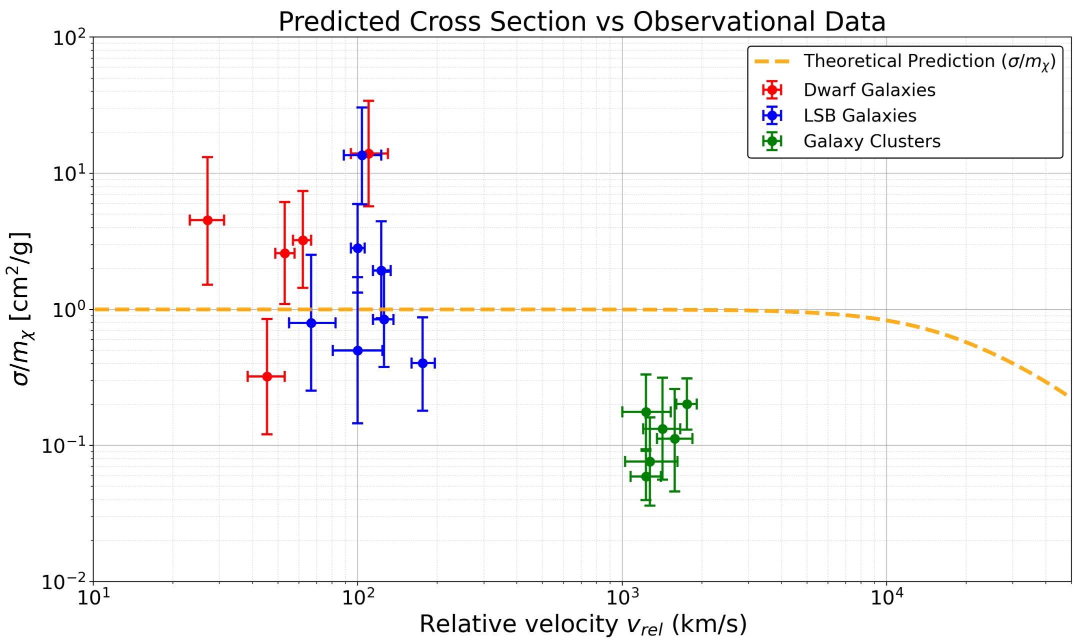

Figure 2.3: *Predicted self-interacting dark matter cross-section σ/m_χ as a function of the relative velocity v_{rel}. The dashed orange line represents the exact theoretical prediction (Eq. (2.7)) for $m_\chi = 1$ GeV, $\alpha_\chi = 0.1$, and $m_\phi = 72.4$ MeV. The observational data points, corresponding to dwarf galaxies (red), standard galaxies (blue), and galaxy clusters (green), are taken from [16].*

As illustrated in Fig. 2.3, the theoretical prediction remains essentially constant at $1\ \text{cm}^2/\text{g}$ throughout the majority of the plotted velocity range. Because the calculated mediator mass is relatively large compared to the momentum transfer at these velocities, the interaction remains strictly within the contact regime ($r \ll 1$). Although this choice satisfies the dwarf galaxy constraints, it fails to reproduce the steep cross-section suppression ($\lesssim 0.1$ cm^2/g) required by galaxy cluster observations at higher velocities ($v_{\rm rel} \sim 1000 - 2000$ km/s).

To resolve this discrepancy and obtain the correct velocity dependence, it is necessary to go beyond the perturbative Born approximation. As anticipated, a light force carrier can induce non-perturbative quantum mechanical effects, specifically the Sommerfeld enhancement, that boost the interaction cross-section at low velocities while keeping it suppressed at cluster scales. The description of this phenomenon, along with the solutions of the Schrödinger equation for the relevant interaction potentials, will be discussed in Chapter 3.

Chapter 3

Sommerfeld Enhancement in Dark Matter Models

As anticipated in Sec. 2.4, a light force carrier provides a significant boost to the annihilation and self-interaction cross-sections at low velocities. This phenomenon, known as Sommerfeld enhancement, is the quantum mechanical counterpart of classical gravitational focusing [18][1]. It becomes relevant whenever particles interact via an attractive, long-range potential [2].

In this chapter, we derive this enhancement by solving the Schrödinger equation for two Dark Matter (DM) particles interacting via a potential $V(r)$. The starting point is the two-body time-independent Schrödinger equation for two identical particles of mass m_χ.

By switching to the center-of-mass (CM) frame and focusing on the relative motion, the dynamics of the system are described by an effective particle with reduced mass $\mu = m_\chi/2$.

3.1 Formalism of the Scattering State

To evaluate the enhancement factor, we must first define the boundary conditions of our scattering problem. In the following sections, we will use for the most part the results from [19, Chap. 6]. In the free-particle case ($V(r) = 0$), the incoming state is a free particle, which we can describe as a plane wave traveling in the z-direction:

$$\psi_k^{(0)}(\vec{r}) = e^{ikz} \tag{3.1}$$

In the presence of a localized scattering potential, the total 3D wavefunction must asymptotically become a superposition of the incident plane wave and an outgoing spherical scattered wave. This imposes the boundary condition as $r \to \infty$:

$$\psi_k(\vec{r}) \xrightarrow{r\to\infty} e^{ikz} + f(\theta)\frac{e^{ikr}}{r} \tag{3.2}$$

where $f(\theta)$ is the scattering amplitude.

[1] As a classical analogy, a point particle impinging on a massive body of radius R and escape velocity v_{esc} has an effective cross-section $\sigma = \pi R^2(1 + v_{\text{esc}}^2/v^2)$. At low asymptotic velocities ($v \ll v_{\text{esc}}$), gravity significantly enhances the geometric cross-section. The Sommerfeld effect represents the quantum equivalent of this low-velocity enhancement.

Furthermore, because the interaction potential $V(r)$ is spherically symmetric, the 3D Schrödinger equation can be expanded using separation of variables into a radial and an angular part:

$$\psi_k(r,\theta,\phi) = \sum_{l=0}^{\infty} \sum_{m=-l}^{l} R_{kl}(r) Y_l^m(\theta,\phi) \tag{3.3}$$

where the $Y_l^m(\theta,\phi)$ are the spherical harmonics. Since the incoming plane wave travels along the z-axis, it breaks 3D symmetry but preserves azimuthal symmetry. Therefore, there is nothing in the potential or the initial state that could introduce a dependence on the azimuthal angle ϕ. This constrains the quantum number to $m = 0$.

Given that $Y_l^0(\theta,\phi) \propto P_l(\cos\theta)$, where P_l is the l-th Legendre polynomial, we can express our general solution for a given momentum k as a superposition of partial waves (indexed by the orbital angular momentum l), each weighted by an amplitude coefficient A_l:

$$\psi_k(\vec{r}) = \sum_{l=0}^{\infty} A_l R_{kl}(r) P_l(\cos\theta) \tag{3.4}$$

3.1.1 Asymptotic Behavior of the Radial Functions

To find the coefficients A_l, we must match the asymptotic form of our expansion in Eq. (3.4) with the explicit boundary condition established in Eq. (3.2). By making the substitution $R_{kl}(r) = \chi_{kl}(r)/r$, with the regularity condition $\chi_{kl}(0) = 0$ to ensure the wavefunction remains finite at the origin, the radial Schrödinger equation becomes:

$$\left[-\frac{1}{m_\chi}\frac{d^2}{dr^2} + \frac{l(l+1)}{m_\chi r^2} + V(r)\right]\chi_{kl}(r) = \frac{k^2}{m_\chi}\chi_{kl}(r) \tag{3.5}$$

where we used the relation $E = k^2/m_\chi$ in the center-of-mass frame. For large distances ($r \to \infty$), both the centrifugal force and the localized potential $V(r)$ become negligible, reducing the problem to a 1D free-particle equation:

$$\chi''_{kl} + k^2\chi_{kl} \simeq 0 \tag{3.6}$$

The general solution to this asymptotic equation is a linear combination of incoming and outgoing spherical waves. In the free-particle case ($V(r) = 0$), the solutions are the spherical Bessel functions $j_l(kr)$. At large distances, these functions asymptotically behave as:

$$\chi_{kl}^{(0)}(r) \propto \sin\left(kr - \frac{l\pi}{2}\right) = \frac{1}{2i}\left[e^{i(kr-l\pi/2)} - e^{-i(kr-l\pi/2)}\right] \tag{3.7}$$

The $-l\pi/2$ term is the free-particle phase shift generated by the centrifugal barrier.

When the localized scattering potential $V(r)$ is introduced in Eq. (3.5), it modifies the wavefunction at short distances. However, because $V(r)$ vanishes as $r \to \infty$, the wave must eventually return to a free-particle-like solution. In a purely elastic scattering process, the conservation of probability (unitarity) requires that the incoming and outgoing particle fluxes must be equal. Therefore, the potential cannot influence the incoming spherical wave (e^{-ikr}) arriving from infinity, nor can it change the overall amplitude of the outgoing wave (e^{ikr}). It can only multiply the outgoing wave by a phase factor $e^{2i\delta_l}$[2].

$$\chi_{kl}(r) \propto \frac{1}{2i}\left[e^{i(kr-l\pi/2)}e^{2i\delta_l} - e^{-i(kr-l\pi/2)}\right] = e^{i\delta_l}\sin\left(kr - \frac{l\pi}{2} + \delta_l\right) \tag{3.8}$$

[2]The factor 2 is a convention; see Ref. [19, Sec. 6.4].

Dropping the overall constant phase $e^{i\delta_l}$, which does not affect the physical probability density, we recover the standard phase-shifted representation:

$$\chi_{kl}(r) \xrightarrow{r\to\infty} \sin\left(kr - \frac{l\pi}{2} + \delta_l\right) \tag{3.9}$$

This shows how a single real parameter, the phase shift δ_l, completely captures the physical effect of the scattering potential $V(r)$ relative to the propagation of a free-particle.

By expanding the incoming plane wave e^{ikz} using Rayleigh's formula[3] and equating it term-by-term with the asymptotic form of our scattered wave, the coefficients A_l can be determined to be $A_l = \frac{1}{k}(2l+1)i^l e^{i\delta_l}$. Plugging this result back into our starting *ansatz*, the complete partial-wave expansion for the scattering state is formally determined as:

$$\psi_k(\vec{r}) = \frac{1}{k}\sum_{l=0}^{\infty}(2l+1)i^l e^{i\delta_l} P_l(\cos\theta) R_{kl}(r) \tag{3.10}$$

3.2 The s-wave Dominance and the 1D Equation

To simplify the full 3D scattering problem into a 1D radial equation, we must exploit two distinct physical limits that characterize the Dark Matter interactions in our model: the short-distance nature of annihilation ($r \to 0$) and the low-velocity regime of the halo ($k \to 0$).

First, we account for the interaction at short distances. We consider the general radial Schrödinger equation, expressing Eq. (3.5) back in terms of the original radial function $R_{kl}(r) = \chi_{kl}(r)/r$ [21, Sec. 4.1]. For small r, the energy E and the Yukawa potential $V(r) \propto 1/r$ are completely overwhelmed by the centrifugal term proportional to $1/r^2$. The differential equation is thus dominated by:

$$\frac{d^2R_{kl}}{dr^2} + \frac{2}{r}\frac{dR_{kl}}{dr} - \frac{l(l+1)}{r^2}R_{kl} \simeq 0 \tag{3.11}$$

This differential equation can be solved by substituting a power-law *ansatz* $R_{kl}(r) \sim r^s$, which yields the characteristic equation $s(s+1) = l(l+1)$. Not considering the negative root $s = -(l+1)$ to ensure a finite and physically acceptable wavefunction at the origin, the solutions must scale as:

$$R_{kl}(r) \sim r^l \quad \text{as } r \to 0 \tag{3.12}$$

Because of this r^l scaling, all higher-order partial waves ($l \geq 1$) vanish at the origin ($R_{kl}(0) = 0$). Only the s-wave ($l = 0$) gives a non-zero contribution $R_{k,0}(0) \neq 0$. Since Dark Matter annihilation is effectively a point-like contact interaction occurring at $r = 0$, this guarantees that only the s-wave component of the wavefunction can lead to annihilation.

Second, the kinematics of the low-velocity regime causes a similar restriction. At very low relative velocities, the elastic scattering process is constrained by threshold behavior: as the de Broglie wavelength $\lambda = 1/k$ becomes much larger than the effective range of the potential R, the centrifugal barrier suppresses all partial waves with $l > 0$. In this limit,

[3] For a guided proof, see Exercises 15.2.24 and 15.2.25 in [20].

the phase shifts scale as $\delta_l \sim k^{2l+1}$, leaving the s-wave as the only significant contribution to the scattering state itself[4]

These two combined limits (annihilation requiring $r = 0$ and the interaction occurring at $k \to 0$) ensure that the entire relevant dynamics are uniquely determined by the $l = 0$ radial equation. Since only the $l = 0$ term survives and $P_0(\cos\theta) = 1$, the infinite sum of Eq. (3.10) reduces to a single term at the origin:

$$\psi_k(0) = \frac{1}{k} e^{i\delta_0} R_{k,0}(0) \tag{3.13}$$

By defining the reduced radial wavefunction specifically for the s-wave as $\psi(r) = rR_{k,0}(r)$, the corresponding Schrödinger equation loses the centrifugal term entirely. Incorporating the relative momentum $k = \mu v_{\text{rel}} = \frac{1}{2} m_\chi v_{\text{rel}}$, the asymptotic kinetic term becomes $k^2/m_\chi = \frac{1}{4} m_\chi v_{\text{rel}}^2$. Thus, the simplified one-dimensional form is:

$$\frac{1}{m_\chi}\psi''(r) + \left[\frac{1}{4} m_\chi v_{\text{rel}}^2 - V(r)\right]\psi(r) = 0 \tag{3.14}$$

where v_{rel} denotes the relative velocity between the two interacting particles.

3.3 Definition of the Enhancement Factor

Dark matter annihilation is a localized short-range process that takes place effectively at $r = 0$. Consequently, the annihilation rate is proportional to the probability density of finding the two interacting particles at the exact same location, $|\psi_k(0)|^2$.

The Sommerfeld enhancement factor S is defined as the ratio of this probability density with and without the interaction potential [18]:

$$S = \frac{|\psi_k(0)|^2}{|\psi_k^{(0)}(0)|^2} \tag{3.15}$$

Assuming the free-particle wavefunction is normalized to a plane wave at infinity ($|\psi_k^{(0)}(0)|^2 = 1$), the enhancement factor simply becomes $S = |\psi_k(0)|^2$.

Using our reduced 1D wavefunction $\psi(r) = rR_{k,0}(r)$, we know that near the origin:

$$R_{k,0}(0) = \lim_{r\to 0} \frac{\psi(r)}{r} = \psi'(0) \tag{3.16}$$

Since we are interested in the squared modulus of $\psi_k(0) \propto R_{k,0}(0)$, the overall phase factors can be ignored. Therefore, the Sommerfeld enhancement factor can be computed directly from the derivative of the 1D reduced wavefunction at the origin:

$$S = \frac{|\psi'(0)|^2}{p^2} \tag{3.17}$$

where $p = k = \frac{1}{2} m_\chi v_{\text{rel}}$ is the asymptotic momentum of the relative motion, acting as the normalization factor to ensure $S \to 1$ when $V(r) \to 0$.

[4] It can be shown that in elastic processes the cross-section takes the form $\sigma = \frac{4\pi}{k^2}\sum_{l=0}^{\infty}(2l+1)\sin^2(\delta_l)$. For small phase shifts, the Taylor expansion yields $\sin\delta_l \approx \delta_l$; thus, given the threshold behavior $\delta_l \sim k^{2l+1}$, we find $\sigma_l \sim k^{4l}$. This makes it clear why higher-order partial waves ($l \geq 1$) can be neglected in the $k \to 0$ limit [19, Sec. 6.6].

Beyond its rigorous quantum mechanical definition, it is useful to operationally define the Sommerfeld enhancement. In phenomenological calculations, the enhancement factor S acts as a non-perturbative multiplier to the standard tree-level cross-section (the Born limit). For a given scattering or annihilation process, in the s-wave regime, the fully enhanced cross-section can be factored as [18]:

$$\sigma = S \cdot \sigma_{\text{Born}} \tag{3.18}$$

Alternatively, when solving the Schrödinger equation subject to purely outgoing boundary conditions at infinity, this physical definition can be shown to be mathematically equivalent to evaluating the amplitude ratio:

$$S = \left| \frac{\psi(\infty)}{\psi(0)} \right|^2 \tag{3.19}$$

A proof of this equivalence, exploiting the properties of the Wronskian, can be found in Appendix B.

Finally, the physics of this system is entirely governed by two dimensionless parameters, which compare the particle's velocity and the mediator mass to the characteristic Bohr velocity α_χ:

$$\varepsilon_v = \frac{v_{\text{rel}}}{2\alpha_\chi}, \qquad \varepsilon_\phi = \frac{m_\phi}{\alpha_\chi m_\chi} \tag{3.20}$$

Depending on the relative magnitude of these parameters, the scattering dynamics can be approached through different analytical frameworks. When the mediator is effectively massless compared to the momentum transfer ($\varepsilon_\phi \ll \varepsilon_v$), the system reduces to a pure Coulomb interaction, a regime we will explicitly solve in Sec. 3.4. In contrast, to describe the finite-range effects of a massive mediator ($\varepsilon_\phi \neq 0$) without relying on computationally expensive numerical integrations, we can analytically approximate the exact Yukawa force using the Hulthén potential. We will explore this approach in Sec. 3.5.

3.4 The Coulomb Limit Approximation

Although the literature often states the exact solution in terms of hypergeometric functions [18], it is instructive to explicitly derive this result to understand how asymptotic boundary conditions model the enhancement factor. Although the standard asymptotic matching of partial wave analysis is inapplicable to the infinite-range Coulomb potential, the physical conclusion that only the s-wave penetrates the origin at low velocities remains true. Thus, we can drop the centrifugal term and focus entirely on solving the exact $l = 0$ radial equation. To solve Eq. (3.14), we must first define the shape of the interaction potential $V(r)$. If the mediator of the Dark Matter interaction is massless ($m_\phi = 0$), the interaction has an infinite range. In this limit, the general Yukawa potential reduces to a simple, un-screened Coulomb potential:

$$V(r) = -\frac{\alpha}{r} \tag{3.21}$$

where α is the coupling constant of the interaction (in our case $\alpha = \alpha_\chi$). Substituting this potential into our reduced radial equation Eq. (3.14), we obtain:

$$\frac{1}{m_\chi}\psi''(r) + \frac{\alpha_\chi}{r}\psi(r) = -\frac{1}{4} m_\chi v_{\text{rel}}^2 \psi(r) \tag{3.22}$$

3.4.1 Adimensionalization and Asymptotic Behavior

To simplify the resolution, it is convenient to introduce a new set of variables. We define a dimensionless distance x and the velocity parameter ε:

$$x = \alpha_\chi m_\chi r, \quad \text{and} \quad \varepsilon = \varepsilon_v = \frac{v_{\text{rel}}}{2\alpha_\chi} \tag{3.23}$$

Applying this change of variables to Eq. (3.22), we obtain the following differential equation:

$$-\psi''(x) - \frac{1}{x}\psi(x) = \varepsilon^2\psi(x) \tag{3.24}$$

where the prime now denotes differentiation with respect to x. Consequently, the Sommerfeld enhancement factor defined in Eq. (3.17) can be expressed in terms of the new variable as $S = |\psi'(0)/\varepsilon|^2$.

To find a suitable *ansatz* for the solution, we must examine the asymptotic behavior of Eq. (3.24) at the boundaries.

- For $x \to \infty$: The potential term $1/x$ becomes negligible, and the equation simplifies to:

$$x \to \infty \implies \psi''(x) \simeq -\varepsilon^2\psi(x) \tag{3.25}$$

  As expected for a free particle far from the interaction center, the solution is a plane wave, $\psi(x) \sim e^{i\varepsilon x}$.

- For $x \to 0$: Conversely, as $x \to 0$, the potential term dominates over the constant energy term ε^2. In order to satisfy the regularity condition $\psi(0) = 0$ to keep the physical wavefunction finite, the dominant linear term implies that $\psi(x) \sim x$ near the origin.

To interpolate between these two asymptotic limits, we can suggest the general structure of the solution to the differential equation by factoring out the known behaviors. We introduce a new unknown function $f(x)$ through the following *ansatz*:

$$\psi(x) = C\, x\, e^{i\varepsilon x} f(x) \tag{3.26}$$

where C is a normalization constant to be determined later.

3.4.2 The Confluent Hypergeometric Equation

By calculating the first and second derivatives of our *ansatz* and substituting them back into Eq. (3.24), the exponential and linear terms factor out, leaving a differential equation for $f(x)$:

$$xf''(x) + (2 + 2i\varepsilon x)f'(x) + (1 + 2i\varepsilon)f(x) = 0 \tag{3.27}$$

We can bring this equation into a standard form by performing the substitution $z = -2i\varepsilon x$. The derivatives transform as $d/dx = -2i\varepsilon(d/dz)$, leading to:

$$zf''(z) + (2 - z)f'(z) - \left(1 - \frac{i}{2\varepsilon}\right) f(z) = 0 \tag{3.28}$$

This is exactly Kummer's equation, also known as the confluent hypergeometric differential equation, whose standard form is $zf'' + (b - z)f' - af = 0$ [22]. By direct comparison, our parameters are:

$$a = 1 - \frac{i}{2\varepsilon} \quad \text{and} \quad b = 2 \tag{3.29}$$

The most general solution is a linear combination of Kummer's function $M(a, b, z)$ and Tricomi's function $U(a, b, z)$. However, the function $U(a, b, z)$ exhibits a singularity at the origin ($z = 0$), which violates our physical regularity condition. Therefore, it must be abandoned. The physical solution is entirely described by Kummer's function:

$$\psi(x) = C\,x\,e^{i\varepsilon x} M\left(1 - \frac{i}{2\varepsilon}, 2, -2i\varepsilon x\right) \tag{3.30}$$

3.4.3 Normalization and Final Result

The final step is to determine the normalization constant C to match the standard scattering boundary conditions at infinity, $\psi(x) \to \sin(\varepsilon x + \delta)$. We can exploit the asymptotic expansion of $M(a, b, z)$ for large $|z|$:

$$M(a, b, z) \xrightarrow{|z|\to\infty} \frac{\Gamma(b)}{\Gamma(a)} e^z z^{a-b} + \frac{\Gamma(b)}{\Gamma(b-a)} (-z)^{-a} \tag{3.31}$$

Substituting our parameters a and b, one can perform the algebraic reduction to extract the sinusoidal phase shift and match the amplitude to unity. As detailed in Appendix C, it can be shown that C is determined by the Gamma functions evaluated at the complex parameter a. Specifically, $|C| \propto |\Gamma(1 - i/2\varepsilon)|$.

To compute the Sommerfeld enhancement, we must evaluate the derivative of the wave-function at the origin. Since $M(a, b, 0) = 1$ by definition, the derivative $\psi'(0)$ acts only on the linear term x, leaving simply $\psi'(0) = C$. Therefore, the enhancement factor is proportional to $|C|^2$:

$$S = \frac{|C|^2}{\varepsilon^2} = \left|\frac{\Gamma(1 - i/2\varepsilon)}{\varepsilon}\right|^2 \times \text{(normalization factors)} \tag{3.32}$$

The product of the Gamma functions can be resolved using Euler's formula: $\Gamma(z)\Gamma(1-z) = \pi/\sin(\pi z)$, combined with the identity $\sin(ix) = i\sinh(x)$. This manipulation allows the complex Gamma functions to simplify into a real exponential, yielding the exact Sommerfeld enhancement factor for the Coulomb potential:

$$S = \frac{\pi/\varepsilon}{1 - e^{-\pi/\varepsilon}} = \frac{2\pi\alpha_\chi/v_{\rm rel}}{1 - e^{-2\pi\alpha_\chi/v_{\rm rel}}} \tag{3.33}$$

To verify the physical validity of Eq. (3.33), we can analyze its asymptotic behavior in the high-velocity and low-velocity limits:

- **High-velocity limit** ($\varepsilon \to \infty$, or $v_{\rm rel} \gg \alpha_\chi$): The exponent π/ε approaches zero. By expanding the exponential to first order ($e^{-x} \simeq 1 - x$), the denominator becomes π/ε. This cancels the numerator, yielding $S \to 1$. As expected, at high velocities the kinetic energy dominates over the potential, and the enhancement effect completely vanishes.
- **Low-velocity limit** ($\varepsilon \to 0$, or $v_{\rm rel} \ll \alpha_\chi$): The exponent π/ε approaches infinity, causing the exponential term $e^{-\pi/\varepsilon}$ to vanish. The denominator approaches unity, and the enhancement grows inversely proportional to the velocity, $S \simeq 2\pi\alpha_\chi/v_{\rm rel}$. This leads to the substantial cross-section amplifications characteristic of cold Dark Matter halos.

3.5 The Hulthén Potential

As discussed in the previous sections, the exact physical interaction between DM particles is mediated by a massive dark photon, which gives rise to the Yukawa potential introduced in Eq. (2.5). Unlike the massless Coulomb case analyzed in Sec. 3.4, the finite mass of the mediator m_ϕ introduces an exponential screening factor $e^{-m_\phi r}$ that limits the range of the force.

However, the radial Schrödinger equation does not admit a general closed-form analytical solution for the exact Yukawa potential. To avoid relying solely on computationally expensive numerical integrations, it is useful to approximate the Yukawa interaction with the attractive Hulthén potential [23]:

$$V_H(r) = -\frac{\alpha_\chi \delta e^{-\delta r}}{1 - e^{-\delta r}} \tag{3.34}$$

where the Hulthén screening mass δ is related to the physical mediator mass m_ϕ by $\delta = \kappa m_\phi$. Here, κ is an $\mathcal{O}(1)$ numerical constant, typically set to $\kappa = \pi^2/6 \approx 1.64$ to match the exact asymptotic behavior [24].

This potential is of primary importance because it admits an exact analytical solution to the s-wave Schrödinger equation while correctly approximating the physical limits of the Yukawa force: it reproduces the $1/r$ Coulomb-like singularity at short distances ($r \ll m_\phi^{-1}$) and exhibits the required exponential screening at large distances ($r \gg m_\phi^{-1}$). The discrepancy between the two potentials is maximal in the intermediate region $r \sim m_\phi^{-1}$, but this introduces a relatively minor error in the calculation of the cross-section, mathematically reduced by the parameter choice for κ [23].

In this section, we will derive the exact expression for the scattering phase shift and the corresponding cross-section as outlined in [23, Appendix A].

First, we substitute the expression for the Hulthén potential, Eq. (3.34), into the radial 1D Schrödinger equation (Eq. (3.14)):

$$\frac{1}{m_\chi}\psi''(r) + \left[\frac{1}{4}m_\chi v_{\rm rel}^2 + \frac{\alpha_\chi \kappa m_\phi e^{-\kappa m_\phi r}}{1 - e^{-\kappa m_\phi r}}\right]\psi(r) = 0 \tag{3.35}$$

Now, we introduce a set of dimensionless variables:

$$x = \alpha_\chi m_\chi r, \quad a = \frac{v_{\rm rel}}{2\alpha_\chi}, \quad c = \frac{\alpha_\chi m_\chi}{\kappa m_\phi} \tag{3.36}$$

such that Eq. (3.35) simplifies to:

$$\frac{d^2\psi}{dx^2} + \left[a^2 + \frac{c^{-1}e^{-x/c}}{1 - e^{-x/c}}\right]\psi(x) = 0 \tag{3.37}$$

In order to solve this differential equation, a change of variables is needed:

$$t = 1 - e^{-x/c} \implies e^{-x/c} = 1 - t \tag{3.38}$$

It is important to notice the boundaries: $x \to 0$ corresponds to $t \to 0$, while $x \to \infty$ corresponds to $t \to 1$. Applying the chain rule, the spatial derivatives transform as:

$$\frac{d}{dx} = \frac{1-t}{c}\frac{d}{dt}, \qquad \frac{d^2}{dx^2} = \frac{(1-t)^2}{c^2}\frac{d^2}{dt^2} - \frac{1-t}{c^2}\frac{d}{dt} \tag{3.39}$$

Substituting these operators into Eq. (3.37), the differential equation takes the form:

$$\frac{(1-t)^2}{c^2}\frac{d^2\psi}{dt^2} - \frac{1-t}{c^2}\frac{d\psi}{dt} + \left[a^2 + \frac{c^{-1}(1-t)}{t}\right]\psi(t) = 0 \tag{3.40}$$

To solve Eq. (3.40), we must factor out the required boundary behaviors. The wavefunction must vanish at the origin ($t = 0$), meaning $\psi \propto t$, and it must behave as a free plane wave $e^{\pm iax}$ at infinity ($t \to 1$), which in the new variable corresponds to $(1-t)^{\pm iac}$. Hence, we express the general solution through the following *ansatz*:

$$\psi(t) = t(1-t)^{iac} f(t) \tag{3.41}$$

Substituting this *ansatz* back into Eq. (3.40) and expanding the derivatives, specific terms cancel out: the asymptotic kinetic term a^2 is canceled by the derivatives of the $(1-t)^{iac}$ factor, while the $1/t$ divergence at the origin is regularized by the linear factor t. After factoring out the common overall component $t(1-t)^{iac}$, the resulting differential equation for the residual function $f(t)$ simplifies exactly into the standard Euler's hypergeometric differential equation:

$$t(1-t)\frac{d^2 f}{dt^2} + [2 - (\lambda_+ + \lambda_- + 1)t]\frac{df}{dt} - \lambda_+\lambda_- f(t) = 0 \tag{3.42}$$

where the constant parameters λ_+ and λ_- are identified as:

$$\lambda_\pm \equiv 1 + iac \pm \sqrt{c - a^2c^2} \tag{3.43}$$

We can rewrite these coefficients in terms of our original physical variables by substituting the definitions of a and c:

$$\lambda_\pm = 1 + \frac{im_\chi v_{\rm rel}}{2\kappa m_\phi} \pm \sqrt{\frac{\alpha_\chi m_\chi}{\kappa m_\phi} - \frac{m_\chi^2 v_{\rm rel}^2}{4\kappa^2 m_\phi^2}} \tag{3.44}$$

The exact solution to this differential equation, provided that it is regular at the origin $t = 0$, is given by the Gaussian hypergeometric function ${}_2F_1(\lambda_+, \lambda_-; 2; t)$. Therefore, the final solution for the reduced radial wavefunction takes the form:

$$\psi(t) = t(1-t)^{iac}\, {}_2F_1(\lambda_+, \lambda_-; 2; t) \tag{3.45}$$

up to an overall constant normalization factor.

To find the physical scattering phase shift δ_0, we must examine the asymptotic behavior of Eq. (3.45) at large distances ($x \to \infty$), which corresponds to evaluating the limit for $t \to 1$. Using the standard connection formulas for hypergeometric functions [23], ${}_2F_1$ evaluated near $t = 1$ can be decomposed into a linear combination of terms proportional to $(1-t)^{-iac}$ and $(1-t)^{iac}$. Returning to the spatial variable x, the asymptotic wavefunction splits into incoming and outgoing plane waves:

$$\psi(x) \xrightarrow{x\to\infty} C_1 e^{-iax} + C_2 e^{iax} \tag{3.46}$$

where the complex coefficient ratio associated with the outgoing wave is determined by the Gamma functions of the hypergeometric parameters:

$$\frac{C_2}{C_1} = \frac{\Gamma(\lambda_+ + \lambda_- - 2)\Gamma(2 - \lambda_+ - \lambda_-)}{\Gamma(\lambda_+)\Gamma(\lambda_-)} \tag{3.47}$$

By matching the structure of Eq. (3.46) to the standard asymptotic form of an s-wave scattering state, $\psi(x) \propto \sin(ax + \delta_0) \propto e^{i(ax+\delta_0)} - e^{-i(ax+\delta_0)}$, the outgoing phase shift δ_0 is isolated as the phase of the coefficient C_2. This yields:

$$\delta_0 = \arg\left(\frac{i\Gamma(\lambda_+ + \lambda_- - 2)}{\Gamma(\lambda_+)\Gamma(\lambda_-)}\right) \tag{3.48}$$

Recalling our definitions for $\lambda_\pm$, we can simplify the argument of the numerator. Since the sum of the roots is $\lambda_+ + \lambda_- = 2 + 2iac$, we find $\lambda_+ + \lambda_- - 2 = 2iac = im_\chi v_{\rm rel}/\kappa m_\phi$. Substituting this back, we obtain the exact phase shift:

$$\delta_0 = \arg\left(\frac{i\Gamma\left(\frac{im_\chi v_{\rm rel}}{\kappa m_\phi}\right)}{\Gamma(\lambda_+)\Gamma(\lambda_-)}\right) \tag{3.49}$$

Finally, with the analytical expression for the phase shift δ_0, we can compute the interaction cross-section. As discussed in Sec. 3.2, to assume that the scattering is dominated entirely by the s-wave contribution, the characteristic momentum of the particles must be much smaller than the potential screening scale, which establishes the strict kinematic limit $m_\chi v_{\rm rel} \ll m_\phi$. Within this low-velocity regime, we can use the $l = 0$ partial-wave formula:

$$\sigma_T \approx \frac{4\pi}{k^2} \sin^2 \delta_0 \tag{3.50}$$

Identifying the relative momentum as $k = \mu v_{\rm rel} = \frac{1}{2} m_\chi v_{\rm rel}$, we arrive at the final non-perturbative cross-section for the Hulthén potential:

$$\sigma_T^{\text{Hulthén}} = \frac{16\pi}{m_\chi^2 v_{\rm rel}^2} \sin^2 \delta_0 \tag{3.51}$$

which is equivalent to the standard result reported in [23].

3.6 Mediator Mass and Consistency Checks

Having derived more refined cross-section expressions in the previous sections, specifically by approximating the Yukawa potential with the Coulomb limit in Sec. 3.4 and employing the Hulthén potential in Sec. 3.5, we first test them against a standard benchmark scenario. We evaluate the models using the parameters $\alpha_\chi = 0.1$ and $m_\chi = 1$ GeV, targeting a dwarf galaxy cross-section of $\sigma/m_\chi \approx 1$ cm^2/g at a characteristic scale $v_{\rm rel} \approx 3 \times 10^{-5} c$[5].

For the Coulomb case, evaluating the enhancement factor S_C at the target velocity yields a massive boost of $S_C \approx 1.05 \times 10^4$. By plugging together Eq. (3.18) and Eq. (2.7), we can solve for the required mediator mass:

$$m_\phi^C \approx 0.7321 \text{ GeV} \tag{3.52}$$

Before using this result, we must test its validity. The Coulomb approximation assumes a massless-like mediator, requiring $m_\phi \ll \alpha_\chi m_\chi$. With our benchmark parameters, the Bohr

[5] Astrophysical literature often parameterizes halo kinematics via the 1D velocity dispersion σ_v. Assuming a Maxwell-Boltzmann velocity distribution [11, Sec. 7.B], the mean relative velocity is $\langle v_{\rm rel}\rangle = \frac{4}{\sqrt{\pi}}\sigma_v \approx 2.26\sigma_v$ (as explicitly derived in Appendix A). Since they differ only by an $\mathcal{O}(1)$ factor, we safely use $v_{\rm rel}$ directly for our order-of-magnitude estimates.

momentum is $\alpha_\chi m_\chi = 0.1$ GeV. Since $m_\phi^C \approx 0.73$ GeV > 0.1 GeV, this initial assumption is vastly violated. To suppress the enormous Sommerfeld enhancement back to the target cross-section, the system requires a heavy mediator, which contradicts the infinite-range premise of the Coulomb limit. Thus, the Coulomb approximation is mathematically inconsistent in this regime.

For the Hulthén potential, calculating m_ϕ requires inverting the s-wave cross-section formula (Eq. 3.51). Matching the target $\sigma_T^{\text{Hulthén}}/m_\chi \approx 1$ cm^2/g yields:

$$m_\phi^H \approx 0.1022 \text{ GeV} \tag{3.53}$$

Checking this against the Hulthén assumptions, the pure s-wave regime requires the characteristic momentum transfer to be well below the screening scale: $m_\chi v_{\text{rel}} \ll m_\phi$. At the dwarf scale, this momentum is $m_\chi v_{\text{rel}} \approx 1 \text{ GeV} \times (3 \times 10^{-5}) = 3 \times 10^{-5}$ GeV, which is orders of magnitude smaller than 0.1022 GeV. Therefore, unlike the Coulomb case, the Hulthén framework is mathematically consistent. The plot of the resulting cross-sections is shown in Fig. 3.1.

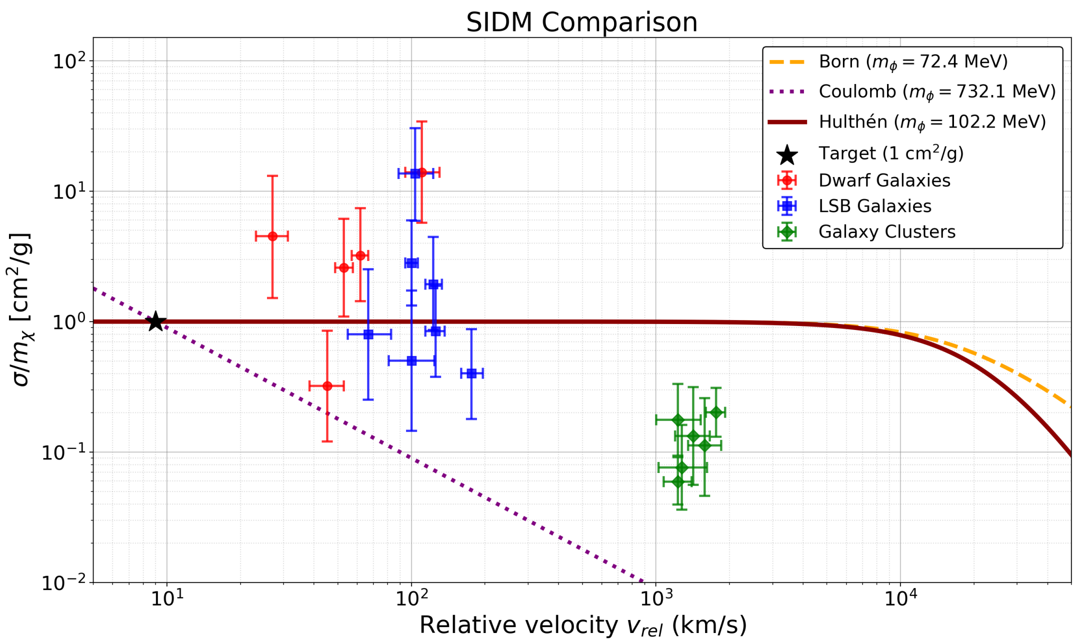

Figure 3.1: *Comparison of the predicted cross-sections for $m_\chi = 1$ GeV and $\alpha_\chi = 0.1$ against astrophysical data. The models are calibrated to target the typical dwarf galaxy cross-section (black star). Although the Hulthén s-wave approximation is mathematically consistent with the kinematic assumptions at the target velocity, the Coulomb limit violates its massless mediator premise. Regardless of their internal mathematical consistency, as the relative velocity increases, all theoretical models remain trapped in the contact regime, failing to reproduce the cross-section suppression required by galaxy clusters.*

However, to understand if this benchmark is physically viable, we must look at how it behaves at the scale of galaxy clusters. In clusters, relative velocities reach $v_{\text{rel}} \sim 1000$ km/s ($\sim 3 \times 10^{-3} c$), raising the momentum transfer to $m_\chi v_{\text{rel}} \approx 3 \times 10^{-3}$ GeV. Notice that this momentum is still much smaller than the required mediator mass (3 MeV $\ll$ 102 MeV).

Physically, a kinetic transition to the suppressed Rutherford regime ($\propto 1/v_{\text{rel}}^4$) occurs only when the momentum transfer overcomes the mediator mass ($v_{\text{rel, crit}} \sim m_\phi/m_\chi$). For this benchmark, $v_{\text{rel, crit}} \approx 0.1c \approx 30{,}000$ km/s, a velocity largely above those of our interest. Accordingly, even at cluster velocities, the interaction remains entirely in the contact regime. With this choice of parameters, our model cannot correctly describe the steep velocity dependence required by cosmological observations.

3.7 A possible Velocity-Dependent Solution

As demonstrated by the 1 GeV benchmark, reproducing the observed halo diversity requires the kinetic transition to fall strictly between dwarf and cluster velocity scales. To achieve this, a different parameter regime must be explored. Following the comprehensive numerical analysis by Kaplinghat et al. [16], we adopt the following benchmark parameters:

$$m_\chi = 15 \text{ GeV}, \quad m_\phi = 17 \text{ MeV}, \quad \alpha_\chi \approx 1/137 \tag{3.54}$$

However, applying the pure s-wave Hulthén formula to these exact parameters reveals an incorrect behavior at high velocities. Specifically, as the relative velocity approaches the cluster scales ($v_{\text{rel}} \gtrsim 500 - 1000$ km/s), the analytical cross-section for $m_\phi = 17$ MeV exhibits a steep dip.

The appearance of this sharp drop is a known quantum mechanical feature of s-wave scattering, specifically an anti-resonance. At certain kinematic points, the phase shift δ_0 crosses a multiple of π, causing the $l = 0$ cross-section to vanish due to destructive interference [25]. However, this deep minimum is unphysical in the complete scattering picture. At these high velocities the momentum transfer approaches and exceeds the mediator mass ($m_\chi v_{\text{rel}} \gtrsim m_\phi$). Consequently, the pure $l = 0$ partial wave alone is no longer sufficient to describe the entire interaction: higher partial waves ($l \geq 1$) successfully overcome the centrifugal barrier and compensate for the s-wave suppression, contributing significantly to the scattering.

To overcome this limitation and accurately describe the physics across all kinematic scales, it is possible to phenomenologically calibrate our effective mediator mass to $m_\phi = 50$ Mev, shifting the parameters away from the anti-resonance to achieve an optimal fit. To represent this, we construct an illustrative analytical model by performing an asymptotic matching: we take the maximum between the exact s-wave Hulthén solution (valid at low velocities) and the perturbative Born approximation (valid at high velocities), using the cross-section formula previously introduced in Eq. (2.7).

It is important to address a subtlety regarding the validity of this model. The strict perturbative condition for the Born regime ($\alpha_\chi m_\chi / m_\phi \ll 1$) is not formally satisfied for the chosen benchmark parameters. Therefore, rather than a rigorous analytical derivation, we employ the Born formula as a phenomenological proxy to estimate the general scaling trend of the high-velocity Rutherford tail ($\propto 1/v_{\text{rel}}^4$), where higher partial waves dominate the interaction. The validity of this approach is explicitly confirmed by its agreement with the full numerical integrations of the Schrödinger equation performed by Kaplinghat et al. [16]. Furthermore, using a simple maximum function to join the Hulthén and Born curves is an illustrative mathematical shortcut adopted in this work to visually capture the transition between the two regimes. Although this phenomenological matching provides a valid fit to the asymptotes, it remains an approximation. A mathematically rigorous description of the intermediate kinematic region, where higher partial waves gradually activate, cannot be captured by this simple maximum function. It requires either the full numerical integration of the exact Schrödinger equation, as performed by Kaplinghat et al. [16], or the derivation of more advanced analytical connection formulas, both of which are beyond the scope of this thesis.

The final result is illustrated in Fig. 3.2. The red dash-dotted line represents the pure s-wave Sommerfeld-enhanced Hulthén solution for $m_\phi = 17$ MeV, clearly showing the anti-resonant dip where the s-wave approximation breaks down. The gray dotted line demonstrates the Born matching applied to this same mediator mass. For the calibrated benchmark ($m_\phi = 50$ MeV), the pure Born limit is isolated as the blue dotted line to explicitly show the classical Rutherford tail. Finally, the purple dashed line represents the final Model: it connects the two asymptotes, smoothly transitioning from the low-velocity resonant regime to the high-velocity perturbative Born limit.

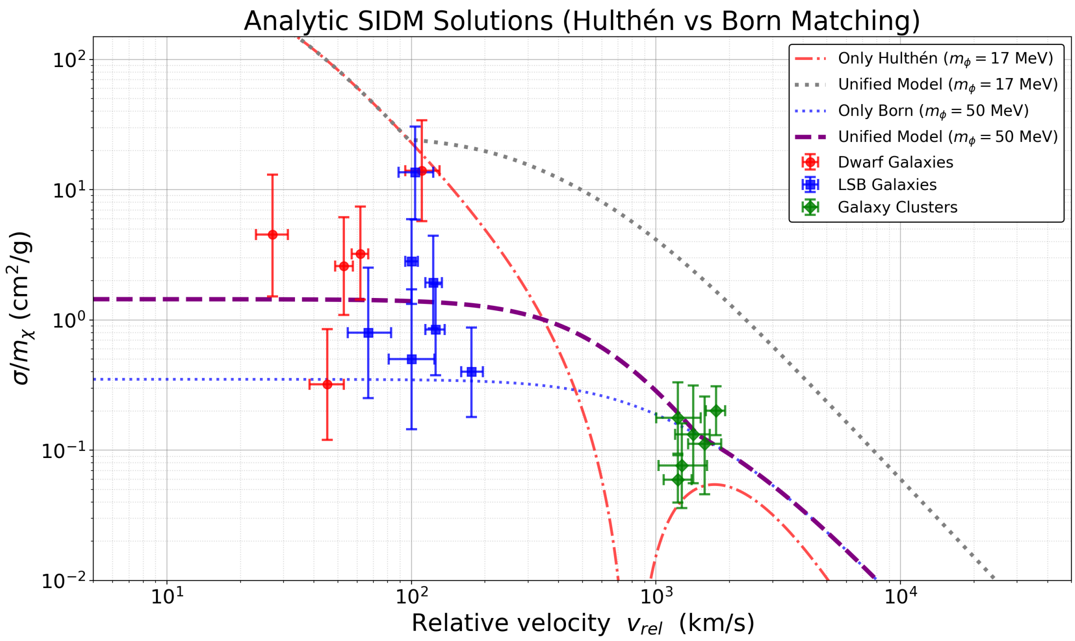

Figure 3.2: *Comparison of analytical SIDM cross-section models against observational data for a benchmark Dark Matter mass $m_\chi = 15$ GeV and $\alpha_\chi \approx 1/137$. The red dash-dotted line shows the exact s-wave Hulthén solution for $m_\phi = 17$ MeV, which drops to zero at high velocities due to a quantum anti-resonance. The gray dotted line illustrates the phenomenological Born matching for this same mass, incorporating higher partial waves but overshooting the data. The blue dotted line isolates the pure Born (Rutherford) limit for a heavier, calibrated mediator ($m_\phi = 50$ MeV). Finally, the purple dashed line represents our Unified Model ($m_\phi = 50$ MeV), constructed by phenomenologically connecting the s-wave Hulthén regime at low velocities (dwarf galaxies) with the Born asymptote at high velocities (galaxy clusters), successfully reconciling the entire kinematic range.*

The physical mechanism behind this fit is now clearer. In dwarf galaxies ($v_{\rm rel} \sim 30$ km/s), the momentum is much smaller than the mediator mass ($m_\chi v_{\rm rel} \ll m_\phi$): the interaction is in the contact regime, where the Sommerfeld enhancement provides the necessary large cross-section ($\sigma/m_\chi \simeq 1-2$ cm^2/g) through the s-wave scattering. At galaxy cluster scales ($v_{\rm rel} \sim 1000$ km/s), the momentum rises enough to resolve the finite range of the potential ($m_\chi v_{\rm rel} \gtrsim m_\phi$). The interaction exits the contact regime, higher partial waves become relevant, and the cross-section drops steeply following the Born approximation, intercepting the cluster data points.

3.8 Conclusion

In conclusion, by identifying the kinematic breakdown of the s-wave approximation at cluster velocities and matching it with the perturbative Born limit, we constructed an illustrative phenomenological model. This approach demonstrates that a velocity-dependent self-interaction framework can, in principle, reconcile some small-scale puzzles across vastly different observable mass scales: from the large core-forming cross-sections in dwarf galaxies to the strictly suppressed interactions in galaxy clusters.

However, it is crucial to interpret these results with a degree of realism, as this model relies on several significant theoretical approximations. First, the Hulthén potential is a mathematical proxy for the exact Yukawa interaction, carrying small deviations at intermediate distances. Second, joining the pure s-wave limit with the high-velocity Born approximation via a phenomenological matching is a useful mathematical shortcut, but it remains an approximation. Although effective, it misses the rigorous computation of the intermediate kinematic regime, where higher-order partial waves ($l \geq 1$) gradually activate and contribute to the scattering process.

Despite these limitations, this analytical framework remains a valuable tool. It successfully captures the essential underlying physics, such as the non-perturbative resonances at low velocities and the Rutherford-like suppression at high velocities, without the need for computationally expensive numerical integrations. Future developments of this analytical method will require connection formulas in the intermediate kinematic region and a more complete expansion of the cross-section at cluster velocities.

Finally, while exact numerical solutions of the Yukawa potential across all partial waves already exist in the literature [23, 16] and serve as the standard benchmark, obtaining a definitive picture of the dark sector's dynamics will require a deeper understanding of the interplay between SIDM and baryonic feedback. Only by combining accurate particle physics cross-sections with advanced hydrodynamical simulations will it be possible to definitively resolve the small-scale puzzles of galaxy formation.

Appendix A

Relative Velocity in a Maxwell-Boltzmann Distribution

In astrophysical literature, the kinematic properties of a Dark Matter halo are usually parameterized by its 1D velocity dispersion, σ_v. Assuming the halo has reached local thermal equilibrium through self-interactions, the velocities of the individual DM particles follow a standard Maxwell-Boltzmann distribution.

For a single particle, the 3D probability density function for its velocity vector $\vec{v}$ is given by an isotropic Gaussian distribution:

$$f(\vec{v}) = \left(\frac{1}{2\pi\sigma_v^2}\right)^{3/2} e^{-\frac{v^2}{2\sigma_v^2}} \tag{A.1}$$

When evaluating the self-interaction rate, the relevant kinematic quantity is not the absolute velocity of a single particle, but the relative velocity between two colliding particles, defined as $\vec{v}_{\rm rel} = \vec{v}_1 - \vec{v}_2$.

Since $\vec{v}_1$ and $\vec{v}_2$ are independent random variables, each normally distributed with variance σ_v^2, their difference $\vec{v}_{\rm rel}$ is also a 3D Gaussian random variable. According to the properties of the normal distribution, the variance of the difference of two independent variables is the sum of their variances. Therefore, the relative velocity vector has a variance $\sigma_{\rm rel}^2 = 2\sigma_v^2$.

The probability density function for the relative velocity vector is then:

$$f(\vec{v}_{\rm rel}) = \left(\frac{1}{4\pi\sigma_v^2}\right)^{3/2} e^{-\frac{v_{\rm rel}^2}{4\sigma_v^2}} \tag{A.2}$$

To find the distribution of the relative speed $v_{\rm rel} = |\vec{v}_{\rm rel}|$, we transition to spherical coordinates in velocity space and integrate over the solid angle ($d^3v_{\rm rel} = 4\pi v_{\rm rel}^2 dv_{\rm rel}$):

$$f(v_{\rm rel}) = 4\pi \left(\frac{1}{4\pi\sigma_v^2}\right)^{3/2} v_{\rm rel}^2 e^{-\frac{v_{\rm rel}^2}{4\sigma_v^2}} \tag{A.3}$$

The mean relative velocity $\langle v_{\rm rel}\rangle$ is the expectation value computed over this distribution:

$$\langle v_{\rm rel}\rangle = \int_0^\infty v_{\rm rel} f(v_{\rm rel})\, dv_{\rm rel} = 4\pi \left(\frac{1}{4\pi\sigma_v^2}\right)^{3/2} \int_0^\infty v_{\rm rel}^3 e^{-\frac{v_{\rm rel}^2}{4\sigma_v^2}}\, dv_{\rm rel} \tag{A.4}$$

The integral on the right-hand side is a standard Gaussian integral of the form $\int_0^\infty x^3 e^{-\alpha x^2} dx = \frac{1}{2\alpha^2}$. By substituting $\alpha = 1/(4\sigma_v^2)$, the integral evaluates to $8\sigma_v^4$.

Multiplying this result by the pre-factors, we obtain the exact relation between the mean relative velocity and the 1D velocity dispersion:

$$\langle v_{\mathrm{rel}} \rangle = 4\pi \left(\frac{1}{8\pi^{3/2}\sigma_v^3} \right) \cdot 8\sigma_v^4 = \frac{4}{\sqrt{\pi}}\sigma_v \approx 2.26\,\sigma_v \tag{A.5}$$

This demonstrates that the typical relative velocity characterizing a collision in the DM halo is slightly more than twice the 1D velocity dispersion measured from astronomical observations.

Appendix B

Boundary Conditions and the Wronskian Equivalence

The Sommerfeld enhancement factor S can be defined through the derivative of the wave-function at the origin for a standing wave $\psi_S(r)$ normalized to behave as $\sin(pr+\delta)$ at infinity:

$$S = \frac{|\psi'_S(0)|^2}{p^2} \tag{B.1}$$

Alternatively, it can be computed using a purely outgoing wave $\psi_{\text{out}}(r) \to e^{ipr}$ as:

$$S = \frac{|\psi_{\text{out}}(\infty)|^2}{|\psi_{\text{out}}(0)|^2} = \frac{1}{|\psi_{\text{out}}(0)|^2} \tag{B.2}$$

To prove their equivalence, let $\psi_S(r)$ and $\psi_C(r)$ be two real, linearly independent solutions with asymptotic behaviors $\sin(pr+\delta)$ and $\cos(pr+\delta)$, respectively. Their Wronskian is:

$$W = \psi_S(r)\psi'_C(r) - \psi_C(r)\psi'_S(r) \tag{B.3}$$

Since the Schrödinger equation lacks a first-derivative term, Abel's identity ensures W is constant. Evaluating at $r \to \infty$:

$$W(\infty) = \sin(pr+\delta)[-p\sin(pr+\delta)] - \cos(pr+\delta)[p\cos(pr+\delta)] = -p \tag{B.4}$$

At the origin, with $\psi_S(0) = 0$, we have $W(0) = -\psi_C(0)\psi'_S(0)$. Equating $W(0) = W(\infty)$ yields:

$$\psi'_S(0) = \frac{p}{\psi_C(0)} \tag{B.5}$$

Defining the outgoing wave as $\psi_{\text{out}}(r) = \psi_C(r) + i\psi_S(r)$, we note that $\psi_{\text{out}}(0) = \psi_C(0)$ since $\psi_S(0) = 0$. Thus:

$$\frac{1}{|\psi_{\text{out}}(0)|^2} = \frac{1}{|\psi_C(0)|^2} = \frac{|\psi'_S(0)|^2}{p^2} \tag{B.6}$$

This mathematical equivalence is fundamental for numerical computations: it proves that one can choose to integrate the Schrödinger equation either from the origin outwards (using standing waves) or from infinity inwards (using purely outgoing waves), depending on which method is computationally more stable for the chosen potential.

Appendix C

Asymptotic Matching for the Coulomb Potential

This appendix shows the steps required to match the confluent hypergeometric function to the asymptotic scattering boundary conditions, leading to the analytical expression for the Coulomb Sommerfeld enhancement.

We start from the asymptotic expansion of Kummer's function $M(a, b, z)$ for large $|z|$:

$$M(a,b,z) \xrightarrow{|z|\to\infty} \frac{\Gamma(b)}{\Gamma(a)} e^z z^{a-b} + \frac{\Gamma(b)}{\Gamma(b-a)} (-z)^{-a} \tag{C.1}$$

In our specific case, the parameters are $b = 2$, $a = 1 - i\nu$, and $z = -2i\varepsilon x$, where we have defined the real parameter $\nu = 1/(2\varepsilon)$ for notational convenience. Since $\Gamma(2) = 1$, substituting these into the expansion yields:

$$M \sim \frac{e^{-2i\varepsilon x}}{\Gamma(1-i\nu)} (-2i\varepsilon x)^{-1-i\nu} + \frac{1}{\Gamma(1+i\nu)} (-2i\varepsilon x)^{-1+i\nu} \tag{C.2}$$

To construct the full spatial wavefunction $\psi(x)$, we must multiply this expansion by our initial ansatz pre-factor, $Cxe^{i\varepsilon x}$. Notice that the linear term x cancels the x^{-1} terms arising from the expansion, while the exponential terms combine:

$$\psi(x) \sim \frac{C}{2i\varepsilon} \left[\frac{e^{i\varepsilon x}(2i\varepsilon x)^{i\nu}}{\Gamma(1+i\nu)} - \frac{e^{-i\varepsilon x}(-2i\varepsilon x)^{-i\nu}}{\Gamma(1-i\nu)} \right] \tag{C.3}$$

Next, we resolve the complex powers by writing the imaginary unit in polar form: $i = e^{i\pi/2}$ and $-i = e^{-i\pi/2}$. This produces a purely real exponential suppression factor, $e^{-\pi\nu/2}$, along with a logarithmic phase shift $\Theta(x) = \varepsilon x + \nu \ln(2\varepsilon x)$. Collecting these terms, the wavefunction becomes:

$$\psi(x) \sim \frac{C\, e^{-\pi\nu/2}}{2i\varepsilon} \left[\frac{e^{i\Theta(x)}}{\Gamma(1+i\nu)} - \frac{e^{-i\Theta(x)}}{\Gamma(1-i\nu)} \right] \tag{C.4}$$

Expressing the complex Gamma function in polar form as $\Gamma(1 - i\nu) = |\Gamma(1 - i\nu)|e^{i\delta_\Gamma}$, the terms inside the brackets reduce to Euler's definition of the sine function:

$$\psi(x) \sim \frac{C\, e^{-\pi\nu/2}}{\epsilon|\Gamma(1-i\nu)|} \sin\left(\varepsilon x + \nu \ln(2\varepsilon x) + \delta_\Gamma\right) \tag{C.5}$$

The standard scattering boundary condition dictates that the asymptotic standing wave must have an amplitude of exactly unity. Imposing this condition requires the entire pre-factor of the sine function to be equal to 1, completely fixing the magnitude of the normalization constant:

$$|C| = \varepsilon\, e^{\pi\nu/2} |\Gamma(1 - i\nu)| \tag{C.6}$$

Finally, the Sommerfeld enhancement factor is defined as $S = |C|^2/\varepsilon^2$. Squaring our expression for $|C|$ gives:

$$S = e^{\pi\nu} |\Gamma(1 - i\nu)|^2 \tag{C.7}$$

The modulus squared of the Gamma function evaluated at a complex argument can be resolved analytically using Euler's reflection formula, $|\Gamma(1 - i\nu)|^2 = \Gamma(1 - i\nu)\Gamma(1 + i\nu) = \pi\nu/\sinh(\pi\nu)$. Substituting this identity, we obtain:

$$S = e^{\pi\nu} \frac{\pi\nu}{\sinh(\pi\nu)} = e^{\pi\nu} \frac{2\pi\nu}{e^{\pi\nu} - e^{-\pi\nu}} = \frac{2\pi\nu}{1 - e^{-2\pi\nu}} \tag{C.8}$$

Recalling our initial definition $\nu = 1/(2\varepsilon)$, we have $2\pi\nu = \pi/\varepsilon$. The substitution provides the exact analytical formula for the Coulomb potential:

$$S = \frac{\pi/\varepsilon}{1 - e^{-\pi/\varepsilon}} \tag{C.9}$$

Bibliography

[1] Gianfranco Bertone and Dan Hooper. History of dark matter. *Rev. Mod. Phys.*, 90:045002, 2018. [1605.04909].

[2] Marco Cirelli, Alessandro Strumia, and Jure Zupan. Dark Matter. 2024. Preprint, [2406.01705].

[3] D. H. Rogstad and G. S. Shostak. Gross properties of five Scd galaxies as determined from 21-Centimeter observations. *The Astrophysical Journal*, 176:315–321, 1972.

[4] Kenneth C. Freeman. On the Disk-Halo Structure of Spiral Galaxies. *The Astrophysical Journal*, 160:811–830, 1970.

[5] Katherine Freese. Review of Observational Evidence for Dark Matter in the Universe. *Int. J. Mod. Phys. D*, 26(06):1730026, 2017. [1701.01840].

[6] K. G. Begeman, A. H. Broeils, and R. H. Sanders. Extended rotation curves of spiral galaxies: dark haloes and modified dynamics. *Mon. Not. Roy. Astron. Soc.*, 249:523, 1991.

[7] Fritz Zwicky. Die Rotverschiebung von extragalaktischen Nebeln. *Helvetica Physica Acta*, 6:110–127, 1933. [Traduzione inglese in: *Gen. Relativ. Gravit.* **41**, 207–224 (2009)].

[8] Fritz Zwicky. On the masses of nebulae and of clusters of nebulae. *The Astrophysical Journal*, 86:217–246, 1937.

[9] Douglas Clowe, Maruša Bradač, Anthony H. Gonzalez, Maxim Markevitch, Scott W. Randall, Christine Jones, and Dennis Zaritsky. A direct empirical proof of the existence of dark matter. *The Astrophysical Journal*, 648(2):L109, 2006. [astro-ph/0608407].

[10] Mordehai Milgrom. A modification of the Newtonian dynamics as a possible alternative to the hidden mass hypothesis. *The Astrophysical Journal*, 270:365–370, 1983.

[11] Sean Tulin and Hai-Bo Yu. Dark Matter Self-interactions and Small Scale Structure. *Phys. Rept.*, 730:1, 2018. [1705.02358].

[12] David N. Spergel and Paul J. Steinhardt. Observational evidence for self-interacting cold dark matter. *Physical Review Letters*, 84(17):3760–3763, 2000. [astro-ph/9909386].

[13] Miguel Rocha, Annika HG Peter, James S Bullock, Manoj Kaplinghat, Shea Garrison-Kimmel, Jose Onorbe, and Riccardo Valli. Cosmological simulations with self-

interacting dark matter - I. Halo shapes and galaxy cluster observables. *Monthly Notices of the Royal Astronomical Society*, 430(1):81–104, 2013. [1208.3025].

[14] Annika HG Peter, Miguel Rocha, James S Bullock, and Manoj Kaplinghat. Cosmological simulations with self-interacting dark matter - Ii. Halo shapes, radials profiles, and subhalos. *Monthly Notices of the Royal Astronomical Society*, 430(1):105–120, 2013. [1208.3026].

[15] Maxim Markevitch, Anthony H Gonzalez, Douglas Clowe, Alexey Vikhlinin, William Forman, Christine Jones, Stephen Murray, and William Tucker. Direct constraints on the dark matter self-interaction cross section from the merging galaxy cluster 1e 0657-56. *The Astrophysical Journal*, 606(2):819, 2004. [astro-ph/0309303].

[16] M. Kaplinghat, S. Tulin, and H.-B. Yu. Dark Matter Halos as Particle Colliders: Unified Solution to Small-Scale Structure Puzzles from Dwarfs to Clusters. *Phys. Rev. Lett.*, 116:041302, 2016. [1508.03339].

[17] Sudhakantha Girmohanta and Robert Shrock. Cross Section Calculations in Theories of Self-Interacting Dark Matter. *arXiv preprint*, 2022. [2206.14395].

[18] Nima Arkani-Hamed, Douglas P. Finkbeiner, Tracy R. Slatyer, and Neal Weiner. A Theory of Dark Matter. *Phys. Rev. D*, 79:015014, 2009. [0810.0713].

[19] Jun John Sakurai and Jim Napolitano. *Modern Quantum Mechanics*. Cambridge University Press, 3rd edition, 2020.

[20] George B. Arfken, Hans J. Weber, and Frank E. Harris. *Mathematical Methods for Physicists: A Comprehensive Guide*. Academic Press, 7th edition, 2012.

[21] David J. Griffiths and Darrell F. Schroeter. *Introduction to Quantum Mechanics*. Cambridge University Press, 3rd edition, 2018.

[22] NIST Digital Library of Mathematical Functions. `https://dlmf.nist.gov/`. Release 1.2.6 of 2026-03-15.

[23] Sean Tulin, Hai-Bo Yu, and Kathryn M. Zurek. Beyond Collisionless Dark Matter: Particle Physics Dynamics for Dark Matter Halo Structure. *Phys. Rev. D*, 87:115007, 2013. [1302.3898].

[24] S. Cassel. Sommerfeld factor for arbitrary partial wave processes. *Journal of Physics G: Nuclear and Particle Physics*, 37(10):105009, 2010. [0903.5307].

[25] Sean Tulin, Hai-Bo Yu, and Kathryn M. Zurek. Resonant dark forces and small-scale structure. *Phys. Rev. Lett.*, 110, 2013. [1210.0900].